Radiation Field Inside a Reactor of Glass-Fiber Meshes Coated with TiO_2

Carlos R. Esterkin, Antonio C. Negro, Orlando M. Alfano, and Alberto E. Cassano
Instituto de Desarrollo Technológico para la Industria Química
Universidad Nacional del Litoral (UNL) and CONICET, (3000) Santa Fe, Argentina

A photocatalytic reactor for treating polluted gaseous streams was developed with a flat-plate configuration and parallel, glass-fiber meshes coated with TiO_2. It was irradiated from both sides with UV light provided by tubular lamps placed at both sides of the reactor. The first step in the description of the reactor performance is the knowledge of the local values of radiation intensities. The radiation field was modeled by special adaptation of the ray-tracing technique. The model uses two optical properties of the glass-fiber meshes: transmittance and reflectance. To validate the mathematical description of the reactor with experiments, the exiting radiative flux from one side was measured using a precise UV detector. Predictions show a maximun error of 8.3% with respect to experimental values measured at the center of the apparatus. This description of the radiation distribution is indispensable to model the photooxidation reaction.

Introduction

Understanding the radiation field in photocatalytic reactors is an important step toward the modeling of these reacting systems that are usually applied in the photooxidation of organic pollutants in water or air. The catalyst particles, TiO_2 in its different varieties, are usually suspended in the fluid phase, immobilized on a preferably transparent support, or coated on an inert material, thus providing suspended, fluidized, or fixed-bed operations. Since TiO_2 is activated by photon absorption in the UV range, the knowledge of the radiation-field distribution inside the reactor is essential. This is so because in any kinetically controlled photo process, the reaction rate depends, with different functional dependencies, on the local volumetric rate of photon absorption (Cassano et al., 1995), that is, only mass-transfer-controlled reactions are independent of the photon absorption rate.

Even if not conclusively demonstrated, it has been often said that in water environments the largest catalytic efficiency is obtained with solid suspensions (Pozzo et al., 1999). On the other hand, it is also widely recognized that the catalyst separation cost in the treated water militated against this advantage. Thus, the convenience of using different forms of fixed- or fluidized-bed reactors deserves consideration. This approach seems even more imperative for the treatment of contaminated air streams.

The application of the radiative transfer equation (RTE) to the heterogeneous system implies the hypothesis of considering the actual reaction space as a pseudohomogeneous one (Cassano et al., 1995; Esterkin et al., 1998). Then, the complete RTE must be used every time that we are facing a reacting medium that is participative and produces scattering, as in the case of slurries, fluidized-, and even packed-bed reactors. However, not all photocatalytic reactors imply the existence of a participating medium. Some fixed-bed designs based on the use of catalytic walls when applied to cases where the fluid medium is transparent (nonparticipating) to radiation can be rigorously modeled considering radiation exchange between surfaces, as will be shown in this work.

Most of the early work concerning the potential use of photocatalysis in environmental problems dealt with water pollution [see, for example, classic contributions well represented by Schiavello (1985, 1988) and Pelizzetti and Serpone (1986)]. However, in the last decade it seemed clear that applications in air contamination could be even more attractive, mainly because evidence was found that gas-phase photocatalysis is comparatively faster (T-Raissi and Muradov, 1993; Sauer and Ollis, 1996; Noguchi et al., 1998). Hence, a large

Correspondence concerning this article should be addressed to A. E. Cassano.

number of striking realizations are described as already present in the market (Fujishima et al., 1999).

Only a few reports have been published on the modeling of photocatalytic reactors for gas-phase reactions. Communications from Raupp and coworkers are among the most recent (Raupp et al., 1997; Hossain et al., 1999; Changrani and Raupp, 2000). These contributions have been mainly concerned with three different reactors types: a packed-bed reactor made of coated spherical beads, a honeycomb monolith reactor, and a reticulated foam monolithic structure. For the packed-bed reactor with coated spherical beads, a 1-D "two flux" incident model has been used to account for the radial UV light distribution throughout the reactor annular space. The model includes the effect of UV light bypassing the coated support particles, reflection by the catalyst film, and the absorption by and transmission through the absorbing catalyst layers. The radiation-field model for the honeycomb monolith reactors was based on the principles of radiation heat transfer in channels and renders an accurate description of photon flux in terms of geometrically defined differential view factors (Hossain and Raupp, 1998, 1999). The radiation-field model for the reticulated foam photocatalytic reactor has been simulated using Monte Carlo calculations (Changrani and Raupp, 1999). Additional designs are represented by a corrugated-plate photocatalytic reactor configuration as reported by Zhang et al. (2000). Several other reaction arrangements have been used, but no reactor model has been associated with them (for example, membranes fixed on different geometries, and powder-layer reactors with cross-flow operation). With different degrees of approximation, in all cases the existing models have been derived from the fundamentals of radiation transport.

In this work these experiments describe and validate a model of the radiation field inside a fixed-bed photocatalytic reactor made of several parallel plates. Titanium dioxide is immobilized on an inert support formed by a set of parallel planes. These planes (meshes) are constructed with a rigid but porous glass-fiber fabric fixed on a plastic frame. Illumination is produced with UV radiation directed to the catalytic planes through windows made of transparent acrylic (Plexiglas). Activating radiation can be incorporated inside the reactor from one or both windows of the parallelepiped that constitutes the macroscopic reaction space (Figures 1 and 2). Radiation between 300 nm and 400 nm is employed. The reacting fluid is assumed to be transparent within this wavelength range, meaning that the reaction medium does not participate in the radiation exchange and that direct photolysis of the pollutant is nonexistent.

Radiation-Field Model

The radiation field inside this reactor is a typical case where radiation exchange occurs between catalytic surfaces, and the interjacent medium does not influence photon transport. For the modeling, the following hypotheses are made (Esterkin et al., 2000): (1) geometric optics is valid; (2) the windows and meshes of the photoreactor are arranged in a series of parallel planes (Figure 1); these meshes constitute flat, stiff grids that produce diffuse transmission and reflection, as well as absorption of the radiation arriving from all directions; (3) a nonparticipating fluid (transmittance = 100%) exists in the space between meshes; and (4) the most important changes in the radiation field can be approximated with a 1-D model along the x-coordinate. This model will be referred to as the one-dimensional diffuse transmission and reflection model (1-D–DTR model).

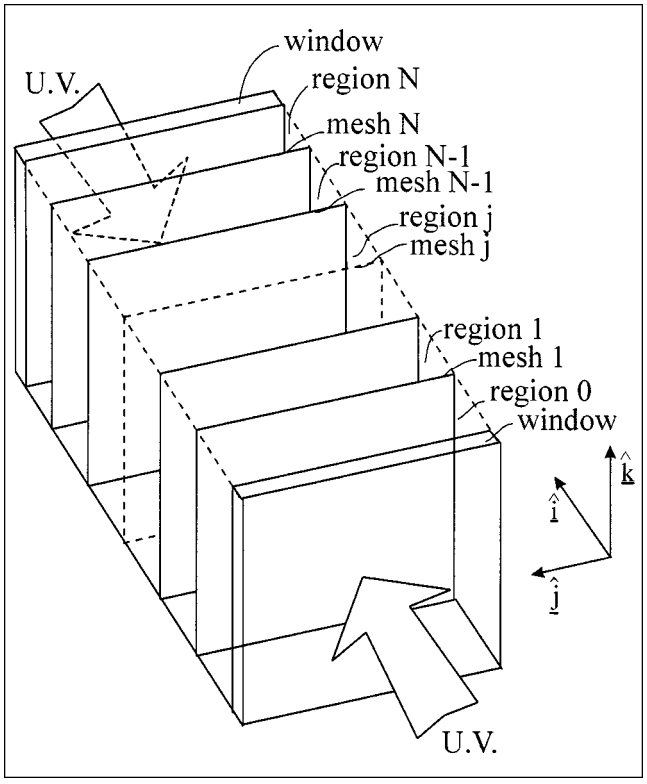

Figure 1. Windows and meshes in the photocatalytic reactor.

Catalytic planes of the reactor are numbered with a generic index j, starting from one of the windows (for example, the front one), and N is the total number of catalytic meshes. Reactor spaces between parallel planes are identified with the number corresponding to the previous mesh. Thus the space between the first window and mesh number 1 receives the number 0, and that between mesh numbers j and $j+1$ is given the number j (Figure 1).

Radiation intensity

At each point, the radiation intensity can be considered the resulting additive effect of two hemispaces of directions, $\hat{\Omega}$, as follows

$$I_j(x, y, z, \hat{\mathbf{\Omega}}) = I_j(x, y, z, \hat{\mathbf{\Omega}}) \left[\theta(\hat{\mathbf{\Omega}} \cdot \hat{\imath}) + \theta(-\hat{\mathbf{\Omega}} \cdot \hat{\imath})\right]$$

$$= I_j^+(x, y, z, \hat{\mathbf{\Omega}})\, \theta(\hat{\mathbf{\Omega}} \cdot \hat{\imath}) + I_j^-(x, y, z, \hat{\mathbf{\Omega}})\theta(-\hat{\mathbf{\Omega}} \cdot \hat{\imath})$$

$$(j = 0, 1, \ldots, N) \quad (1)$$

In Eq. 1 $\theta(s)$ is the step function, j is the generic region, I_j^+ is the hemispace of intensities having "forward directions," and I_j^- is the one corresponding to "backward directions."

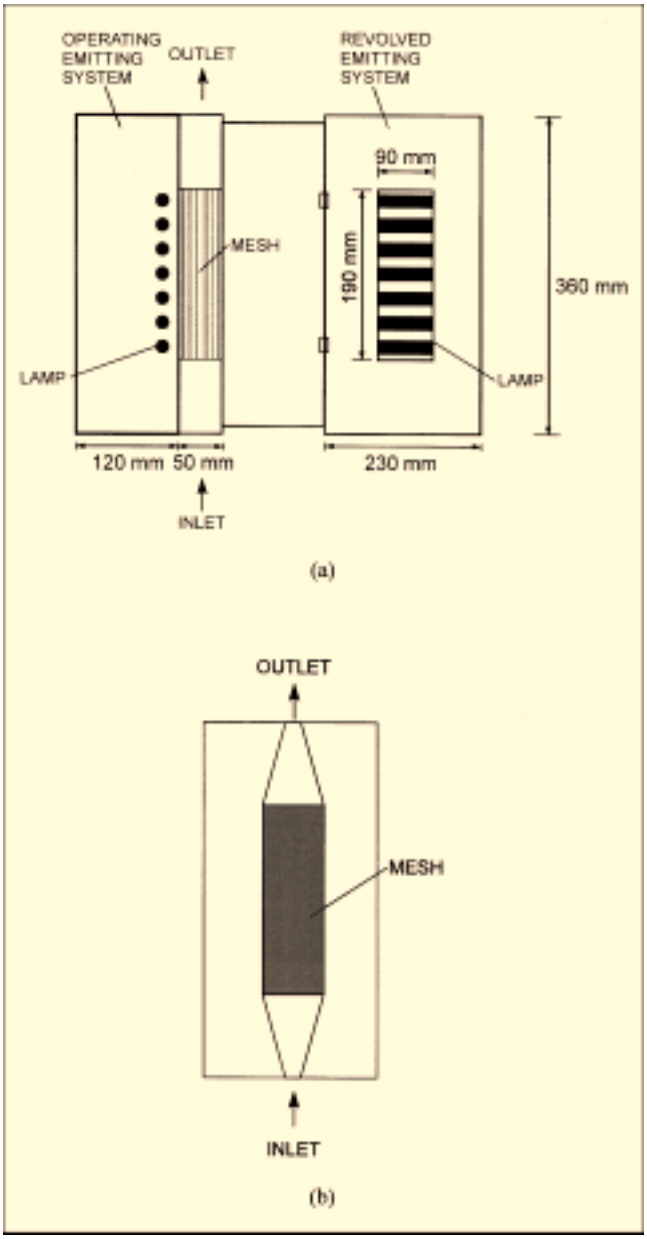

Figure 2. Emitting system and reactor: (a) lateral view; (b) front view.

Intensities between meshes are independent of x because the reaction space is transparent. However, intensities inside each region between meshes are different because radiation is reflected, absorbed, and transmitted by the photocatalytic planes. Hence, at each generic region, j, Eq. 1 results

$$I_j(x, y, z, \hat{\Omega}) = I_j(y, z, \hat{\Omega}) = I_j^+(y, z, \hat{\Omega})\ \theta(\hat{\Omega}\cdot\hat{i}) + I_j^-(y, z, \hat{\Omega})\theta(-\hat{\Omega}\cdot\hat{i}) \qquad (j = 0, 1, \ldots, N) \quad (2)$$

Note that I_j^+ and I_j^- are a function of y and z. This is because, even if the lamps were all exactly equal (which is almost impossible for commercial lamps) due to the geometry

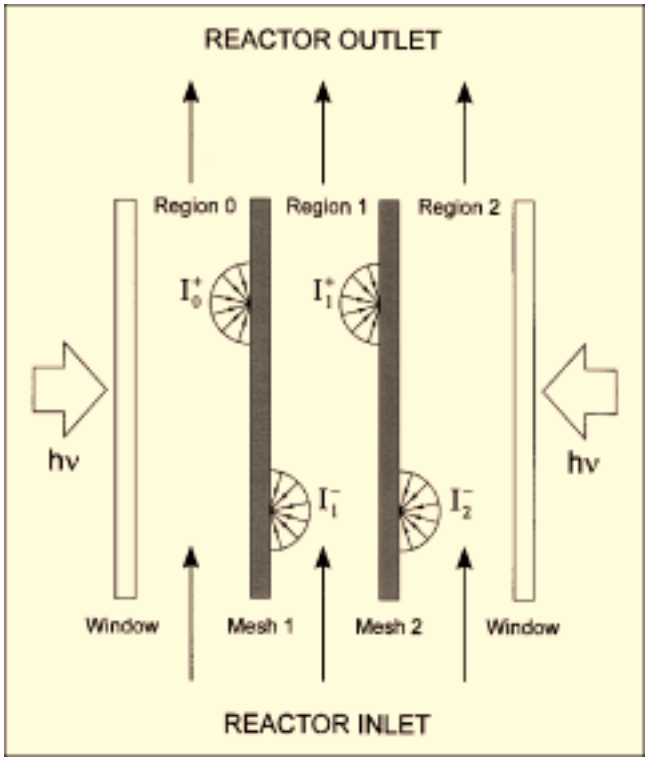

Figure 3. Impinging radiation intensity on each mesh.

of the system, the inlet radiation is not uniform on the plane of radiation entrance. This is a direct consequence of the fact that the illuminating system and the meshes have finite dimensions in the y and z directions and the lamps are tubular emitters along the y-coordinate. In practice, other nonuniformities will be present because the coated meshes will not very likely have uniform optical properties on the whole surface. However, as shown below, these last differences are not taken into account by the model that uses a single value for the reflection and transmission parameters. A two-mesh reactor can be used as an illustrative example for developing the model. Figure 3 shows the impinging radiation intensity on each side of the reacting planes.

Incident radiation

Using the well-known definition of the incident radiation, its value results

$$G_j(y, z) = \int_{4\pi} I_j(y, z, \hat{\Omega})\, d\Omega = \int_{2\pi^+} I_j^+(y, z, \hat{\Omega})\theta(\hat{\Omega}\cdot\hat{i})\, d\Omega + \int_{2\pi^-} I_j^-(y, z, \hat{\Omega})\theta(-\hat{\Omega}\cdot\hat{i})\, d\Omega = G_j^+(y, z) + G_j^-(y, z) \quad (j = 0, 1, \ldots, N) \quad (3)$$

In Eq. 3 $d\Omega$ indicates the differential solid angle.

Radiative-flux vector

From its definition, the radiative flux vector can be expressed as

$$\begin{aligned}\boldsymbol{q}_j(y,z) &= \int_{4\pi} I_j(y,z,\hat{\boldsymbol{\Omega}})\hat{\boldsymbol{\Omega}}\, d\Omega \\ &= \int_{2\pi^+} I_j^+(y,z,\hat{\boldsymbol{\Omega}})\theta(\hat{\boldsymbol{\Omega}}\cdot\hat{\boldsymbol{i}})\hat{\boldsymbol{\Omega}}\, d\Omega \\ &+ \int_{2\pi^-} I_j^-(y,z,\hat{\boldsymbol{\Omega}})\theta(-\hat{\boldsymbol{\Omega}}\cdot\hat{\boldsymbol{i}})\hat{\boldsymbol{\Omega}}\, d\Omega \\ &= \boldsymbol{q}_j^+(y,z) + \boldsymbol{q}_j^-(y,z) \quad (j=0,1,\ldots,N) \end{aligned} \tag{4}$$

It can be shown that for the 1-D–DTR model the following equations are obtained (Appendix A):

$$\begin{aligned} G_j^+ &= 2\pi I_j^+ \\ G_j^- &= 2\pi I_j^- \\ q_j^+ &= \boldsymbol{q}_j^+\cdot\hat{\boldsymbol{i}} = \pi I_j^+ \\ q_j^- &= \boldsymbol{q}_j^-\cdot\hat{\boldsymbol{i}} = -\pi I_j^- \qquad (j=0,1,2,\ldots,N) \end{aligned} \tag{5}$$

where $q_j^{+/-}$ represents the "forward"/"backward" $\hat{\boldsymbol{i}}$-component of the radiative flux vector. These equations are strictly valid if and only if the following conditions are fulfilled: (1) irradiation is uniform in the (z,y) plane of radiation entrance; (2) the Plexiglas windows have uniform optical properties; (3) the catalytic meshes have uniform optical properties; and (4) the meshes and the irradiating plane extend to infinity in the y and z directions. If this is not the case, the 1-D–DTR model is a valid approximation when average values of the incoming radiation fluxes and the optical properties of the different components of the reactor are used in the model.

From Eqs. 3 to 5, we obtain

$$\begin{aligned} G_j &= 2\pi\left[I_j^+ + I_j^-\right] \\ q_j &= \boldsymbol{q}_j\cdot\hat{\boldsymbol{i}} = \pi\left[I_j^+ - I_j^-\right] \end{aligned} \tag{6}$$

Equations 5 and 6 show that for the 1-D–DTR model the usual radiative variables are related in a very simple manner.

Adapted ray-tracing technique

Radiation intensities change upon interaction with the catalytic meshes. Then, the radiation field can be obtained, considering that radiation bundles may (1) undergo partial and diffuse reflection at the catalytic surfaces; (2) be partially absorbed by the coating; (3) be partially and diffusely transmitted through the meshes. The problem can be handled with an adaptation of the ray-tracing technique originally derived for multiple parallel windows (Siegel and Howell, 1992). This work will take into account multiple reflections, absorption, and transmission of radiation in the N meshes and in the entrance/exit windows of the reactor. To calculate the radiation intensity in each region between meshes, we must know all the optical properties of the individual meshes and windows as a function of wavelength. From them, the transmittance, T_j, and reflectance, R_j, of sets of j meshes can be obtained from the following equation hierarchies (Appendix B)

$$\begin{aligned} T_1 &= T \\ T_2 &= \frac{T_1 T_1}{1-R_1R_1} \\ T_3 &= \frac{T_2 T_1}{1-R_2R_1} \\ &\vdots \\ T_N &= \frac{T_{N-1}T_1}{1-R_{N-1}R_1} \end{aligned} \tag{7}$$

$$\begin{aligned} R_1 &= R \\ R_2 &= R_1 + \frac{T_1^2 R_1}{1-R_1R_1} \\ R_3 &= R_1 + \frac{T_1^2 R_2}{1-R_1R_2} \\ R_N &= R_1 + \frac{T_1^2 R_{N-1}}{1-R_1R_{N-1}} \end{aligned} \tag{8}$$

The parameters T and R in Eqs. 7 and 8 represent the transmittance and reflectance of a single mesh. They have been assumed independent of position. They must be obtained from specially designed experiments.

Figure 4 illustrates multiple reflections of the radiation transmitted to region j from the UV radiation sources; I^{0+}

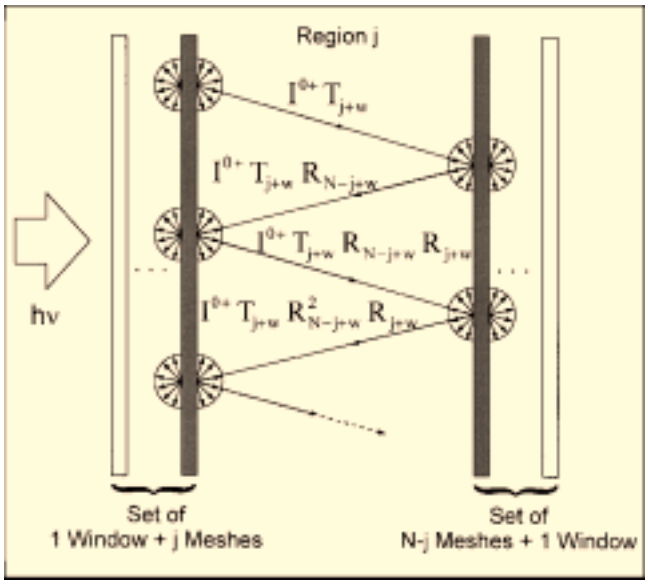

Figure 4. Multiple reflection and transmission of radiation.

represents the "forward" radiation intensity impinging on the entrance window; R_{j+w} and T_{j+w} are the reflectance and transmittance of a set of j meshes and one window; they are related to T_j, R_j and to the transmittance, T_w, and reflectance, R_w, of the windows by the following equations

$$T_{j+w} = \frac{T_j T_w}{1 - R_w R_j}$$

$$R_{j+w} = R_j + \frac{T_j^2 R_w}{1 - R_w R_j} \tag{9}$$

Considering irradiation through only one window, the forward and backward radiation intensities in each j-region are given by

$$I_j^+ = I^{0+} \frac{T_{j+w}}{1 - R_{N-j+w} R_{j+w}}$$

$$I_j^- = I^{0+} \frac{T_{j+w} R_{N-j+w}}{1 - R_{N-j+w} R_{j+w}} \tag{10}$$

Considering irradiation through both windows, I_j^+ and I_j^- result in

$$I_j^+ = I^{0+} \frac{T_{j+w} + T_{N-j+w} R_{j+w}}{1 - R_{N-j+w} R_{j+w}}$$

$$I_j^- = I^{0+} \frac{T_{j+w} R_{N-j+w} + T_{N-j+w}}{1 - R_{N-j+w} R_{j+w}} \tag{11}$$

From Eq. 11 it is straightforward that

$$I_j^+ = I_{N-j}^-$$

$$I_j^- = I_{N-j}^+ \tag{12}$$

Finally, from Eq. 12 and Eq. 6,

$$G_j = G_{N-j}$$

$$q_j = -q_{N-j} \tag{13}$$

Model parameters

The meshes were constructed with a porous glass-fiber fabric. The main features of these meshes are the following: (a) surface mesh density = 0.32 kg/m^2; (b) average fiber diameter = 0.5 $\times$ 10^{-3} m; (c) fiber meshes dimension = 0.09 m width $\times$ 0.19 m length; (d) average mesh thickness = 0.8 $\times$ 10^{-3} m; and (e) surface void fraction = 0.18.

The titania coating (employing Degussa P25) was carried out by means of an immobilization procedure known as "manipulation of a previously made titania powder" (Pozzo et al., 1997). For this work, the Brezovà et al. (1995) technique was used. The glass-fiber fabric was calcined at 400°C for 4 h. Afterwards, the meshes were immersed in a suspension of 5 g/L of TiO_2 in ethanol and kept under good stirring conditions overnight. Finally, the impregnated meshes were dried and calcined for 6 h at 500°C.

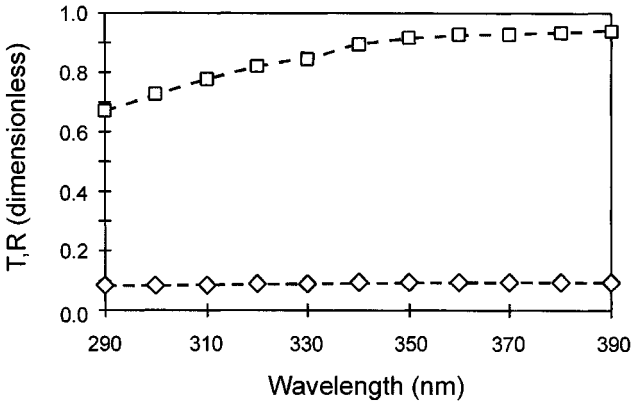

(a)

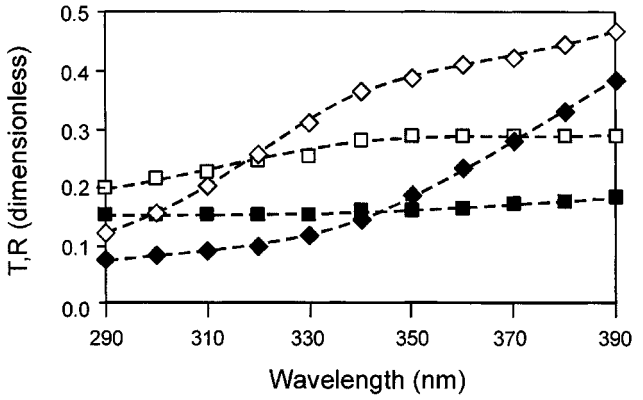

(b)

Figure 5. Transmittance and reflectance experimental values.

(a) Acrylic window, (b) single mesh. Keys: (a) transmittance (□); reflectance (◇); (b) transmittance of uncoated (□) and coated (■) mesh; reflectance of uncoated (◇) and coated (♦) mesh.

The parameters required by the model are the transmittance and reflectance of the meshes (T, R) and those corresponding to the entrance/exit windows of the reactor (T_w, R_w). The values of R and T for a mesh with TiO_2 coating were obtained from experimental data determined as a function of wavelength, between 290 and 390 nm, in a Cary 17 spectrophotometer. The Model 1711, Diffuse Reflectance Accessory was used, which allows diffuse and total reflectance as well as transmittance to be measured. The optical properties of the acrylic windows were determined in the same way. It should be noted that correct evaluation of these properties is essential for bringing forth a deterministic model with no adjustable parameters. Details of the procedure are presented in Appendix C.

Figure 5a and 5b show the experimental results corresponding to reflectance and transmittance measurements of the acrylic reactor window, and a catalytic mesh uncoated

and coated with titanium dioxide, respectively. These results correspond to low catalyst loading, 0.27% in weight having a noncoated support as a reference, or, equivalently, to 0.086 mg of TiO_2/cm^2 of mesh.

From these results the following observations can be made: (1) Plexiglas windows made with the acrylic used (3.2 mm thick) shows good transmission up to 350 nm (better than 90%), while its reflectance is low (less than 10%) with an almost uniform value in the wavelength range of interest. At 290 nm, transmission by the plastic window decreases below 70%. This is not a real problem because other varieties of Plexiglas show a much better performance up to 300 nm and, what is more important, the characteristics of this particular window are properly incorporated into the model. (2) Reflectance by the coated mesh changes from a value close to 40% (at 390 nm) to less than 10% at 290 nm. This trend is in agreement with the expected behavior of the supported titanium dioxide. (3) At first glance, the transmission curve for the coated mesh shows an unexpected result. It indicates a very slow decrease from 390 to 290 nm. This is the result of two main causes: (a) the fabric net made with fiberglass is not compact and part of the light goes through the mesh almost undisturbed regardless of the loading of titanium dioxide, that is, it is closely related to the value corresponding to the fractions of holes in the mesh and thus attributable to the geometric aspects of the glass fabric; (b) a very low loading in the catalytic coating, that is, if titanium dioxide effects would prevail, results should show a sharp increase in absorption (decrease in transmission) below 350 nm; due to the small catalyst concentration, this effect is almost disguised by the absorption and transmission characteristics of the glass-fiber fabric. It is noteworthy that fiberglass meshes with better transmission characteristics will greatly improve the reactor performance.

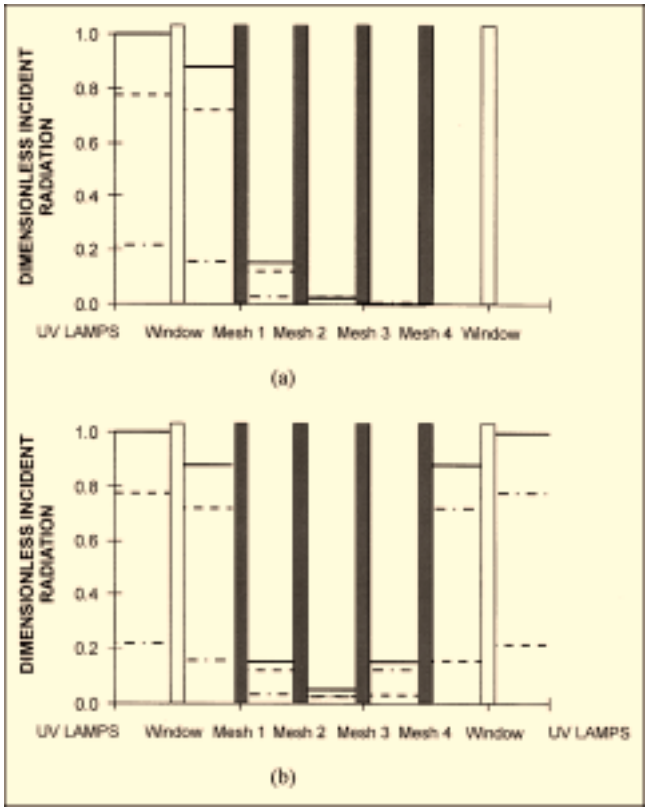

Figure 6. Dimensionless Incident radiation in fixed-bed reactor.

(a) Irradiated from one window (unilateral irradiation); (b) irradiated from both windows (bilateral irradiation). Keys: G_j(—); G_j^+(– – –); G_j^-(– · –).

Computational Results

With the measured data of R and T, the Fortran program starts calculating the reflectance, R_j, and transmittance, T_j, of sets of j meshes for each wavelength, continuing with the calculations of reflectance, R_{j+w}, and transmittance, T_{j+w}, of a set of j meshes and one window. The next step, using the incoming spectral radiation intensity, consists of the computation of the spectral radiation intensity for each region inside the reactor for unilateral or bilateral irradiation. Finally, integration over the range of used wavelengths is performed. The calculations were done with a 300-MHz Pentium II Processor, and the time required for a typical run with four meshes is on the order of 2 s.

Figure 6a shows results for G_j, G_j^+, and G_j^- obtained from the model. They have been made dimensionless using the total incident radiation at the reactor window, and correspond to a reactor with four active meshes and irradiation from only one window. Figure 6b shows the same results, but resulting from irradiation through both windows (employing bilateral irradiation). Table 1 shows numerical results corresponding to both figures.

It can be seen that in both cases (unilateral or bilateral irradiation), the incident radiation experiences an abrupt decrease in the region that follows the first mesh. It becomes clear that the window is almost transparent and that absorption by the coated mesh is significant. For the case illustrated in Figure 6a, the incident radiation in region $j = 1$ is less than 16% of that at the window where radiation enters. As Eq. 13 asserts, and is intuitively expected, in the case of bilateral irradiation the incident radiation shows symmetry with respect to a plane located at the reactor center. Additionally,

Table 1. Dimensionless Incident Radiation in Fixed-Bed Reactor

Region		G	G^+	G^-
Unilateral irradiation				
Entrance		1.000	0.780	0.220
j	0	0.886	0.725	0.161
	1	0.153	0.124	0.029
	2	0.027	0.022	0.005
	3	0.005	0.004	0.001
	4	0.000	0.000	0.000
Exit		0.000	0.000	0.000
Bilateral irradiation				
Entrance		1.000	0.780	0.220
j	0	0.886	0.725	0.161
	1	0.158	0.125	0.033
	2	0.054	0.027	0.027
	3	0.158	0.033	0.125
	4	0.886	0.161	0.725
Exit		1.000	0.220	0.780

bilateral irradiation helps to establish a radiation profile that shows a slight improvement in the desired uniformity along the x-coordinate. This last effect is more noticeable when the reactor has only a few catalytic meshes.

It can be seen that in spite of the previously mentioned small catalyst loading, the radiation field takes on very different values in moving from a reaction space close to the window where radiation enters to the next one. Note, for example, that after two catalytic planes, the incident radiation falls to a value slightly above 5% of the entering radiation. This effect is mainly attributable to the attenuation produced by the support. Undoubtedly the efficiency of the reactor would be greatly improved if a much more transparent mesh had been employed.

The model as it is presented here is useful for providing a good estimate of the maximum number of catalytic meshes that should be used in a particular application, such as to avoid the existence of regions inside the reactor that will be very inefficient or even useless.

Clearly, there is much room for improving the present design. It can be done along the following lines: (1) using a more transparent support by either changing the type of glass or, even better, by altering the pitch of the grid that forms the supporting mesh, and (2) increasing the catalyst loading. It is well known that using a different procedure for immobilizing the catalyst, for example, "*in situ* catalyst generation by the sol gel process" (Pozzo et al., 1997), the catalyst concentration fixed on the support can reach values as high as 10% (in our laboratory, values larger than 7% have been measured). Obviously, the model can also be used to calculate the optimal catalyst concentration for a reactor with a given number or meshes.

Experimental Reactor Characteristics and Measurement of Radiation Field

The photocatalytic reactor was made of an acrylic box (a parallelepiped) that can accommodate from one to six catalytic meshes (Figure 2). A custom-made illuminating system (see below) can irradiate the reactor from both sides through a rectangular-shaped window made of acrylic plastic having a thickness of 3.2 mm. As indicated earlier, this window has a fairly good degree of transparency in the UV range of interest ($290 \text{ nm} \leq \lambda \leq 390 \text{ nm}$).

The illuminating system was made of two metallic boxes that permit the housing and exact positioning of seven blacklight lamps [Philips TL 4W/08 (F4T5/BLB)]. These lamps have emission between 310 nm and 410 nm, with a peak at 350 nm. The boxes with the lamps can be revolved to place the sensor (instead of the lamps) of a UV radiometer by the reactor window and to measure irradiation introduced from the opposite side. Commercial lamps, as received, are uniformly distributed on the rectangular space of illumination and are connected to an instrument panel that permits separate control of the lighting and operation of each lamp.

Measurement of the radiation field was made with a Research UV Radiometer IL 1745 (from International Light), employing an SED 005 detector (GaAsP-type photodiode) with a WBS 320 # 16789 band-pass filter and a W # 7698 wide-eye diffuser made of quartz (42 mm in diameter). The sensor has a spectral range from 250 nm to 400 nm, with a peak response at 350 nm, and has an active area of 5 mm^2. Using the diffuser, the detector follows the "cosine law" directional response. The detector can be precisely located on the surface of the reactor window by means of a device that has measurable movements in the y and z directions. This permits reproducible positioning of the detector in a preestablished 3×5 regular grid (15 different points on the reacting plane).

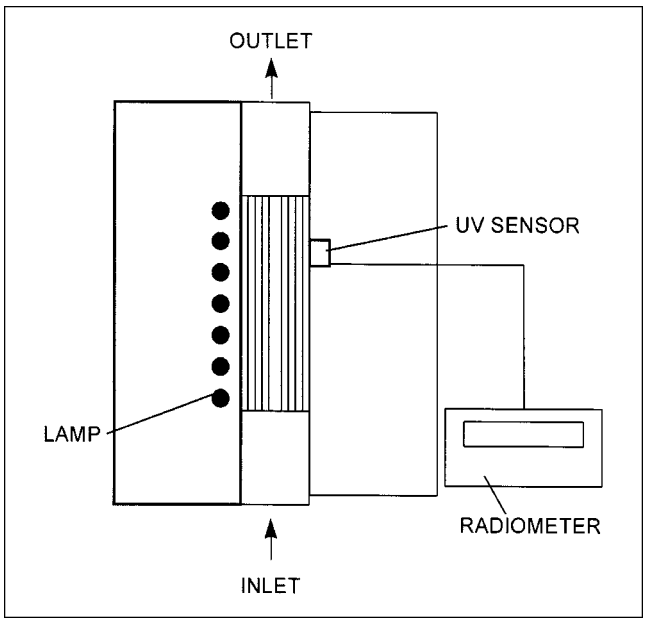

Figure 7. Fixed-bed reactor, and UV sensor and radiometer.

It must be pointed out that the radiative property measured by the detector is the $\hat{i}$-component of the forward radiative flux vector defined in Eq. 5. Proper calibration of the sensor allows the experimental determination of radiative fluxes (measured in terms of current intensities) on the window surface.

Measurements were made on just one side of the reactor (Figure 7) for the following operating conditions:

(1) Without the reactor, at positions corresponding to the exit window facing the radiation sources (type "a" measurement at back window position). At each y-z position, it provides the value of the inlet condition for radiation transport along the x direction.

(2) With an empty reactor (without catalytic meshes) at the same positions, in order to know the effects produced by both acrylic windows (type "b" measurement at back window position).

(3) At the same positions, with the reactor filled with one, two, and three catalytic meshes (type "c" measurements at back window position).

Theoretical Results and Experimental Data

Radiation enters through one window and measurements and calculations are made at the opposite window. The experimental verification of the radiation-field predictions was

made by means of a *direct comparison of current intensities* measured with the radiometer with those *calculated* from the radiation fluxes predicted by the model. It must be noted that comparing current intensities is the most direct way of model verification. The model permits calculation from the spectral distribution of the lamp output power and spectral values of the optical parameters, the spectral distribution of the outgoing radiation fluxes. These fluxes can be directly converted into current intensities from the existing information about the radiometer (spectral and peak response). Conversely, to convert measured current intensities produced by polychromatic irradiation into integrated values of polychromatic fluxes requires a proposal of the spectral distribution corresponding to the experimental outgoing radiation. This distribution cannot be known without using the same information required by the model to calculate the transmitted fluxes. Thus, incorporating these values (to convert the current intensities provided by the detector—and resulting from polychromatic irradiation—into fluxes) could provide a potentially perturbed confirmation of the quality of the predicted values. Fortunately, there is no need for doing it, because the verification can be made by directly comparing current intensities.

To calculate the incoming radiative flux (q_λ^{0+}) at the opposite window position we use: (1) the experimental value of the current intensity given by the radiometer with measures of the type "a"; it gives the value of $i_{0,\exp}$; (2) the normalized spectral distribution of the lamp output power in the UV range (ϵ_λ); (3) the normalized sensitivity of the radiometer provided by the manufacturer [$S_n(\lambda)$]; and (4) the detector sensitivity at the peak response, measured at 350 nm (S_p). Then, the spectral radiative flux q_λ^{0+} is given by (Appendix D)

$$q_\lambda^{0+}(y,z) = i_{0,\exp}(y,z)\frac{\lambda\epsilon_\lambda k}{S_p\int_\lambda S_n(\lambda)\epsilon_\lambda d\lambda} \tag{14}$$

In Eq. 14, λ represents the wavelength and $\lambda \times k$ is a wavelength-dependent factor that transforms watts into moles of photons (Brandi et al., 2000) according to $k = (1/Nhc) = 8.358\times10^{-9}$ einstein$\cdot$s$^{-1}\cdot$W$^{-1}\cdot$nm^{-1}.

Note that $q_\lambda^{0+}(y,z)$ also could have been obtained from an emission model for the seven-lamp illuminating system. In this case, superposition of direct radiation emission from each one of the lamps permits the calculation of intensities at any point on the front space (Cassano et al., 1995). Transforming these intensities into fluxes is a straightforward procedure.

Using the experimentally determined value of q_λ^{0+} as an entrance datum (obtained from Eq. 14), our model predictions permit the calculation of the values of the spectral radiative fluxes at any position (y,z) in the opposite window: $q^+_{\lambda,\mathrm{mod}}(y,z)$, for 0, 1, 2, 3, …, N catalytic meshes along the radiation path. Then, knowing the values of $S_n(\lambda)$ and S_p, with no further assumptions, we can calculate the current intensities corresponding to theoretical predictions of fluxes according to (Appendix E)

$$i_{\mathrm{mod}} = \frac{S_p}{k}\int_\lambda S_n(\lambda)\frac{q^+_{\lambda,\mathrm{mod}}}{\lambda}d\lambda \tag{15}$$

These calculated values can be compared with the experimental values obtained with the radiometer ($i_{\exp}$), employing measurements of types "b" and "c." It is important to remark that application of Eq. 15 does not introduce additional assumptions to those related to the radiation-field model involved in the calculation of $q^+_{\lambda,\mathrm{mod}}$. This direct comparison can be made because, as shown in Appendix E, only theoretical and experimental electrical currents are compared. On the other hand, to validate the model comparing radiation fluxes, additional assumptions concerning the wavelength distribution of the output radiation should have been used to transform the radiometer readings, $i_{\exp}$ (polychromatic), into radiation fluxes.

At this point one may ask the following preliminary questions: (1) How uniform is the irradiation produced by seven commercial lamps that are uniformly distributed in the illuminating system? and (2) How uniform are the coating and the optical properties of the catalytic meshes?

Table 2 shows the experimental values of type "a" measurements of the radiation fluxes expressed in current intensities (reading from the radiometer in microamperes) at different positions on the reactor corresponding to a 3 × 5 measuring grid. Part of these results should have been expected; irradiation produced by the illuminating system cannot be the same at the different heights of the catalytic surface. Moreover, symmetry with respect to the center line will be observed if and only if the output power produced by all the lamps is the same, a fact that would hardly be found in commercial black-light lamps. Thus, it is clear that superimposed on the expected nonuniformities produced by the form of the illuminating system, there is a distortion created by lamps that do not have exactly equal emission characteristics. Clearly, the lamps at the bottom produce stronger irradiation than the ones at the top. Since the model can use different values of $q_\lambda^{0+}(y,z)$, this is not a problem for this reactor where inlet fluxes are experimentally measured. However, this result provides a warning about using the model for scaling-up purposes without properly calibrating the lamps that will be used in the larger system. In the latter, an *a priori* design must use an emission model instead of experimentally measured values of $q_\lambda^{0+}(y,z)$. Then, for this model either it will be assumed that all the lamps have equal emission and neglect the differences, or information concerning the different output powers must be incorporated into it. In any event, for this experimental reactor and in order to avoid the collapse of the one-dimensional (1-D) model, one must assume that (1) either the incoming radiation flux is the result of an averaging procedure, or (2) the model is applied separately to each of the 15 different sections, representing the matrix of

Table 2. Detector Current Intensities Resulting from Irradiation by Seven Lamps ($i_{0,\exp}$)*

Position	Vertical 1	Vertical 2	Vertical 3
Horizontal 1	2.0	2.4	2.1
Horizontal 2	2.8	3.3	2.9
Horizontal 3	3.2	3.6	3.3
Horizontal 4	3.0	3.7	3.2
Horizontal 5	2.3	2.8	2.4

*Absolute values in μA for different positions. No windows and no meshes.

Table 3. Experimental Values of Relative Current Intensities ($i_{exp}/i_{0,exp}$) at Different Reactor Positions*

Position	Vertical 1	Vertical 2	Vertical 3
Horizontal 1	0.115	0.112	0.107
Horizontal 2	0.123	0.120	0.112
Horizontal 3	0.129	0.134	0.117
Horizontal 4	0.132	0.130	0.119
Horizontal 5	0.136	0.134	0.125

Note that nonuniformities in the boundary condition (irradiation from the lamps reported in Table 2) are compensated with the employed procedure to make results reported in this table dimensionless.
*Two windows and one catalytic mesh.

sampling spaces on the catalytic planes. Moreover, it appears that a good predictive model for scaling-up purposes has to be three-dimensional. This would mean some additional computational complexities along the same lines described in this work.

Table 3 shows the results of relative radiation fluxes, expressed in terms of current intensities ($i_{exp}/i_{0,exp}$) for 15 positions on the reactor surface, corresponding to a case that includes the two windows and one catalytic mesh. It is again clear that added to the differences produced by the lamps, changes are introduced by the inexistence of a unique value for the optical properties of the meshes, that is, either the characteristics of the fiberglass fabric or those of the catalyst layer immobilized on the support are not the same for the whole surface of this mesh. From Table 3, it is evident that for positions (2,1), (3,1), and (4,1), the performance of the mesh is different than for positions (2,3), (3,3), and (4,3). (The first number corresponds to the row and the second to the column.) These differences are not taken into account by the one-dimenssional model, but could be minimized if the values of the optical properties used were the average results of several measurements made in different parts of the catalytic plane. Exclusively attributing these additional distortions to the catalytic mesh is the result of supplementary experimental information (not shown here) obtained for relative radiation fluxes corresponding to the reactor with two windows and no meshes. These results indicate that the Plexiglas walls have almost uniform optical properties, that is, it was found that distortions produced by the lamp are not altered by the window plates.

Table 4 presents results corresponding to the validation of the model. It shows a comparison between predictions and experimental values of the relative current intensities. Again, they have been made dimensionless using the value of $i_{0,exp}$.

Table 4. Relative Experimental and Theoretical Currents Intensities*

No. of Meshes	$i_{exp}/i_{0,exp}$	$i_{mod}/i_{0,exp}$	Error (%)
0	0.864	0.825	4.5
1	0.134	0.137	2.2
2	0.022	0.023	4.5
3	0.0036	0.0039	8.3

*Measured at the reactor center.

Values in Table 4 correspond to the case of the detector placed at the center of the reactor window with the empty reactor ($N = 0$) and with a variable number of meshes ($N = 1$, 2, 3). Errors in the model predictions with respect to the experimental values are also reported. It can be seen that the maximum error in the case of the three meshes is 8.3%. For a reactor with three meshes (not very efficient, as seen before) in some regions of the rectangular surface, particularly in two points close to the border, errors as large as 44 and 50% were observed. It has been said that the optical properties of the catalytic surfaces are not uniform. Moreover, these surfaces are not infinite planes, as should be required for a perfect one-dimensional model. Furthermore, employing three meshes, the measured current intensities corresponding to transmitted radiation are very low, and consequently errors are magnified because we approach the recommended detection limit for the instrument. This was seen to be less significant when only one or two catalytic surfaces were used. Additionally, more meshes in the reactor means that errors in the experimental measurements of the R and T values will be increasingly propagated when calculations are performed with the model. Finally, when the single theoretical prediction of the model is compared with the average value of all 15 measurements corresponding to the matrix of experimental points, the error is smaller than 18%.

Conclusions

The main results can be summarized as follows:

- A one-dimensional, diffuse transmission and reflection (1-D−DTR) model to evaluate the radiation field in a photocatalytic reactor made with TiO_2 coated on glass-fiber meshes was developed. This model involves a 1-D, rigorous treatment for this type of fixed-bed photoreactor.
- The optical parameters—reflectance and transmittance of a single mesh and those corresponding to the acrylic windows—were independently and experimentally obtained in order to incorporate them into the radiation-field model.
- The 1-D−DTR model predicts the radiation intensity for each reaction space that exists between the meshes all along the reactor. This result permits estimation of the appropriate number of meshes that are needed in order to avoid reaction-inactive regions inside the reactor. The model can also be used to decide on the optimal catalyst loading for a given number of meshes.
- The obtained results show the convenience of the bilateral irradiation of the reactor in order to produce more uniform incident radiation profiles.
- To validate the model, a method was used that employs the following external information: spectral distribution of the lamp output power, plus spectral and peak responses of the radiometer sensor. Thus, no additional assumptions are needed to compare model predictions with experimental data.
- Good agreement exists between the radiation field predicted by the model and the experimental data. This result enables us to pursue the next step of this work, which will model the reactor with a specific degradation reaction.
- It appears convenient that for scaling-up purposes, in order to account for the nonuniform radiation entrance, a three-dimensional model will be more appropriate.

Acknowledgments

The authors are grateful to CONICET, ANPCyT (PID 22 and FONCyT programs), CyTED, and Universidad Nacional del Litoral for their support of this work. They also thank Paolini S.A.I.C. for providing the acrylic plates and Eng. Claudia Romani for her technical assistance.

Notation

c = speed of light, $m \cdot s^{-1}$
G_j = total incident radiation in region j, einstein $\cdot m^{-2} \cdot s^{-1}$
G_j^+ = forward incident radiation in region j, einstein $\cdot m^{-2} \cdot s^{-1}$
G_j^- = backward incident radiation in region j, einstein $\cdot m^{-2} \cdot s^{-1}$
h = Planck's constant, $J \cdot s$
$i_{0\lambda}$ = spectral current intensity without reactor, $\mu A \cdot nm^{-1}$
$i_{0,\exp}$ = experimental current intensity without reactor, μA
$i_{\exp}$ = experimental current intensity at the exit window of the reactor, μA
i_{mod} = current intensity provided by the model at the exit window of the reactor, μA
I^{0+} = forward radiation intensity at the window of radiation entrance, einstein $\cdot m^{-2} \cdot s^{-1} \cdot sr^{-1}$
I_λ^{0+} = spectral forward radiation intensity at the window of radiation entrance, einstein $\cdot m^{-2} \cdot s^{-1} \cdot sr^{-1} \cdot nm^{-1}$
I_j = radiation intensity in region j, einstein $\cdot m^{-2} \cdot s^{-1} \cdot sr^{-1}$
I_j^+ = forward radiation intensity in region j, einstein $\cdot m^{-2} \cdot s^{-1} \cdot sr^{-1}$
I_j^- = backward radiation intensity in region j, einstein $\cdot m^{-2} \cdot s^{-1} \cdot sr^{-1}$
k = conversion factor from Watt to photochemical units, einstein $\cdot s^{-1} \cdot W^{-1} \cdot nm^{-1}$
N = Avogadro number (6.023×10^{23})
P = lamp output power, W
P_λ = lamp spectral output power, $W \cdot nm^{-1}$
P_P = peak of the lamp output power, W
$\boldsymbol{q}_j$ = radiative flux vector in region j, einstein $\cdot m^{-2} \cdot s^{-1}$
$\boldsymbol{q}_j^+$ = forward radiative flux vector in region j, einstein $\cdot m^{-2} \cdot s^{-1}$
$\boldsymbol{q}_j^-$ = backward radiative flux vector in region j, einstein $\cdot m^{-2} \cdot s^{-1}$
q^{0+} = forward radiative flux without reactor, einstein $\cdot m^{-2} \cdot s^{-1}$
q_λ^{0+} = forward spectral radiative flux without reactor, einstein $\cdot m^{-2} \cdot s^{-1} \cdot nm^{-1}$
$q_{\lambda,\mathrm{mod}}^+$ = forward spectral radiative flux at the exit window provided by the model, einstein $\cdot m^{-2} \cdot s^{-1} \cdot nm^{-1}$
R = reflectance of a single mesh, dimensionless
R_w = reflectance of a single window, dimensionless
S = radiometer sensitivity, $A \cdot m^2 \cdot W^{-1}$
S_p = peak of the radiometer sensitivity, $A \cdot m^2 \cdot W^{-1}$
S_n = normalized radiometer sensitivity, dimensionless
T = transmittance of a single mesh, dimensionless
T_w = transmittance of a single window, dimensionless

Greek letters

ϵ_λ = normalized spectral distribution of the lamp output power, nm^{-1}
λ = wavelength, nm
$\hat{\boldsymbol{\Omega}}$ = unit vector along the ray direction, dimensionless

Literature Cited

Brandi, R. J., O. M. Alfano, and A. E. Cassano, "Evaluation of Radiation Absorption in Slurry Photocatalytic Reactors. 2. Experimental Verification of the Proposed Method," *Environ. Sci. Technol.*, **34**, 2631 (2000).

Brezovà, V., A. Blazkovà, M. Brezñan, P. Kottás, and M. Ceppan, "Phenol Degradation on Glass Fibers with Immobilized Titanium Dioxide Particles," *Collect. Czech. Chem. Commun.*, **60**, 788 (1995).

Cassano, A. E., C. A. Martín, R. J. Brandi, and O. M. Alfano. "Photoreactor Analysis and Design," *Ind. Eng. Chem. Res.*, **34**, 2155 (1995).

Changrani, R., and G. B. Raupp, "Monte Carlo Simulation of the Radiation Field in a Reticulated Foam Photocatalytic Reactor," *AIChE J.*, **45**, 1085 (1999).

Changrani, R., and G. B. Raupp, "Two-Dimensional Heterogeneous Model for a Reticulated-Foam Photocatalytic Reactor," *AIChE J.*, **46**, 829 (2000).

Esterkin, C. R., O. M. Alfano, and H. A. Irazoqui, "An Alternative Approach to the Radiative Transfer Equation for a Solid-Fluid Heterogeneous System," *Lat. Amer. Appl. Res.*, **28**, 151 (1998).

Esterkin, C. R., A. C. Negro, O. M. Alfano, and A. E. Cassano, "Radiation Field Inside a Photocatalytic Reactor with TiO_2 Coated Glass Fiber Meshes," *Proc. of the Intl. Conf. Water Supply and Water Quality*, Kraków, Poland, p. 661 (2000).

Fujishima, A., K. Hashimoto, and T. Watanabe, *TiO_2 Photocatalysis, Fundamentals and Applications*, Bkc Inc., Tokyo (1999).

Hossain, M. M., and G. B. Raupp, "Radiation Field Modeling in a Photocatalytic Monolith Reactor," *Chem. Eng. Sci.*, **53**, 3771 (1998).

Hossain, M. M., and G. B. Raupp, "Polychromatic Radiation Field Model for a Honeycomb Monolith Photocatalytic Reactor," *Chem. Eng. Sci.*, **54**, 3027 (1999).

Hossain, M. M., G. B. Raupp, S. O. Hay, and T. N. Obee, "Three-Dimensional Developing Flow Model for Photocatalytic Monolith Reactors," *AIChE J.*, **45**, 1309 (1999).

Noguchi, T., A. Fujishima, P. Sawunyama, and K. Hashimoto, "Photocatalytic Degradation of Gaseous Formaldehyde Using TiO_2 Film," *Environ. Sci. Technol.*, **32**, 3831 (1998).

Pelizzetti, E., and N. Serpone, eds., *Homogeneous and Heterogeneous Photocatalysis*, Reidel, Dordrecht, The Netherlands (1986).

Pozzo, R. L., M. A. Baltanás, and A. E. Cassano, "Supported Titanium Oxide as Photocatalyst in Water Decontamination: State of the Art," *Catal. Today*, **39**, 219 (1997).

Pozzo, R. L., M. A. Baltanás, and A. E. Cassano, "Towards a Precise Assessment of the Performance of Supported Photocatalysts for Water Detoxification Processes," *Catal. Today*, **54**, 143 (1999).

Raupp, G. B., J. A. Nico, S. Annangi, R. Changrani, and R. Annapragada, "Two-Flux Radiation Model for an Annular Packed-Bed Photocatalytic Reactor," *AIChE J.*, **43**, 792 (1997).

Sauer, M. L., and D. F. Ollis, "Photocatalyzed Oxidation of Ethanol and Acetaldehyde in Humidified Air," *J. Catalysis*, **158**, 570 (1996).

Schiavello, M., ed., *Photocatalysis and Environment*, Kluwer, Dordrecht, The Netherlands (1988).

Schiavello, M., ed., *Photochemistry, Photocatalysis and Photoreactors*, Reidel, Dordrecht, The Netherlands (1985).

Siegel, R., and J. R. Howell, *Thermal Radiation Heat Transfer*, 3rd ed., Hemisphere, Washington, DC, p. 931 (1992).

T-Raissi, A., and N. Z. Muradov, "Flow Reactor Studies of TiO_2 Photocatalytic Treatment of Airborne Nitroglyceryn," *Photocatalytic Purification and Treatment of Water and Air*, D. Ollis and H. Al-Ekabi, eds., Elsevier, Amsterdam, p. 435 (1993).

Zhang, Z., W. A. Anderson, and M. Moo-Young, "Rigorous Modeling of UV Absorption by TiO_2 Films in a Photocatalytic Reactor," *AIChE J.*, **46**, 1461 (2000).

Appendix A

Taking into account that the radiation field model is 1-D, the hypothesis of diffuse transmission and reflection, and considering that incoming radiation fluxes are uniform (or made uniform through an averaging procedure), the spectral radiation intensity in each of the j regions is independent of y, z, and $\hat{\boldsymbol{\Omega}}$. Thus:

$$I_j^{+/-}\left(y,z,\hat{\boldsymbol{\Omega}}\right) = I_j^{+/-} \tag{A1}$$

Equation A1 is valid because we have assumed that $I_0^{+/-} \neq I_0^{+/-}(y,z)$, $R \neq R(y,z)$, and $T \neq T(y,z)$.

According to Eq. 3 and Eq. A1, the forward and backward incident radiation result in

$$G_j^+ = I_j^+ \int_{2\pi^+} d\Omega = I_j^+ \int_0^{\pi/2} \sin\theta d\theta \int_0^{2\pi} d\varphi = 2\pi I_j^+$$

$$G_j^- = I_j^- \int_{2\pi^-} d\Omega = I_j^- \int_{\pi/2}^{\pi} \sin\theta d\theta \int_0^{2\pi} d\varphi = 2\pi I_j^- \tag{A2}$$

Considering Eq. 4, the forward and backward $\hat{i}$-components of the radiative flux vector are given by

$$q_j^+ = \boldsymbol{q}_j^+ \cdot \hat{\boldsymbol{i}} = I_j^+ \int_{2\pi^+} \hat{\boldsymbol{\Omega}} \cdot \hat{\boldsymbol{i}} \, d\Omega$$

$$= I_j^+ \int_0^{\pi/2} \cos\theta \sin\theta d\theta \int_0^{2\pi} d\varphi = \pi I_j^+$$

$$q_j^- = \boldsymbol{q}_j^+ \cdot \hat{\boldsymbol{i}} = I_j^- \int_{2\pi^-} \hat{\boldsymbol{\Omega}} \cdot \hat{\boldsymbol{i}} \, d\Omega$$

$$= I_j^- \int_{\pi/2}^{\pi} \cos\theta \sin\theta d\theta \int_0^{2\pi} d\varphi = -\pi I_j^- \quad \text{(A3)}$$

Appendix B

To illustrate the derivation of Eqs. 7 and 8 in the main text, let us consider the case of a set of two meshes. The radiation intensity I_T that is transmitted by this set can be expressed as

$$I_T = T_2 I_I \quad \text{(B1)}$$

where I_I represents the radiation intensity impinging on the first mesh, and T_2 is the transmittance of the set of two meshes.

I_T also can be obtained as the result of the radiation intensity transmitted through the first mesh, which after multiple reflections on the two meshes, is transmitted through the second mesh (Figure B1a). Then

$$I_T = \left(T_1T_1 + T_1R_1R_1T_1 + T_1R_1^2R_1^2T_1 + T_1R_1^3R_1^3T_1 + \cdots\right) I_I$$

$$= \frac{T_1T_1}{1 - R_1R_1} I_I \quad \text{(B2)}$$

Comparing Eqs. B1 and B2, we conclude that

$$T_2 = \frac{T_1T_1}{1 - R_1R_1} \quad \text{(B3)}$$

In an analogous manner, the radiation intensity that is reflected by the set of two meshes can be written as

$$I_R = R_2 I_I \quad \text{(B4)}$$

where R_2 represents the reflectance of the set of two meshes.

I_R also can be expressed as the result of the transmitted radiation through the first mesh, which returns to the incident region after multiple reflections on the two meshes (Figure B1b)

$$I_R = \left(R_1 + R_1T_1^2 + R_1R_1^2T_1^2 + R_1^2R_1^3T_1^2 + \cdots\right) I_I$$

$$= \left(R_1 + \frac{T_1^2R_1}{1 - R_1R_1}\right) I_I \quad \text{(B5)}$$

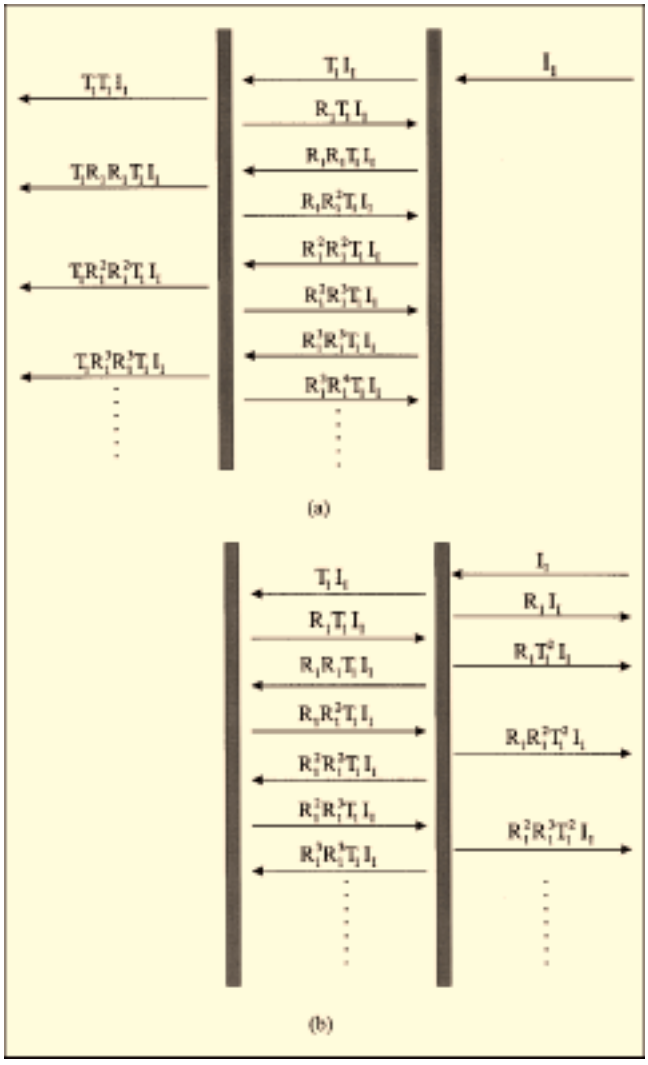

Figure B1. Radiation intensity.

(a) Transmitted by a set of two meshes; (b) reflected by a set of two meshes.

Consequently

$$R_2 = R_1 + \frac{T_1^2R_1}{1 - R_1R_1} \quad \text{(B6)}$$

Appendix C

The diffuse reflectance accessory of the spectrophotometer has been used (Figure C1). It consists of an integrating sphere with five portholes: one for the sample beam, one for the reference beam, one for the detector, one sample port, and one reference port. Pure and fresh MgO is always used as the reference for the integrating sphere. Zero and 100% of the instrument are obtained with a specially made black body and another piece of MgO placed at the sample port, respectively. Plexiglas plates are placed as samples without any special treatment. Coated and noncoated fiberglass meshes are

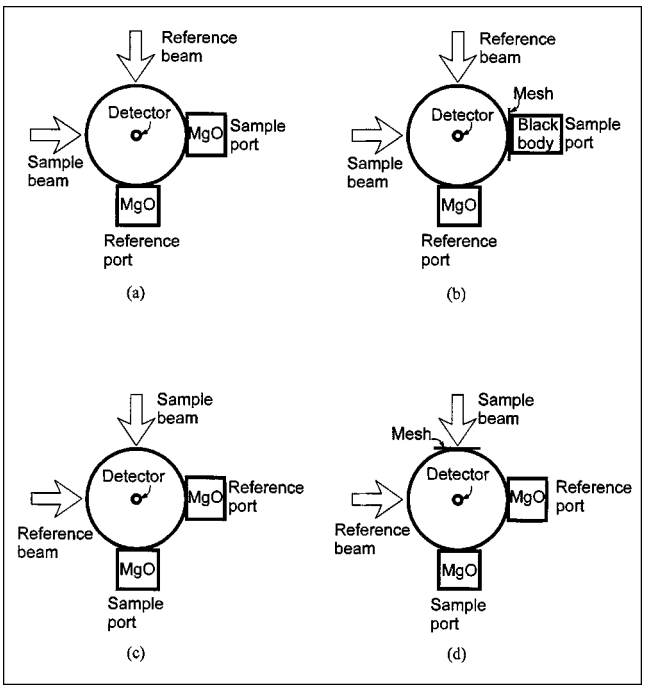

Figure C1. Different configurations of the integrating sphere for measuring optical properties.

(a), (b) Reflectance measurements; (c), (d) transmittance measurements.

mounted in a specially made holder (a frame similar to a slide-holder) to permit correct positioning of the fabric in the sample port.

Total reflectance measurements

As shown in Figure C1b, the sample is placed in the sample port with its back covered by a black body that absorbs all transmitted radiation. Readings in this case correspond to reflectances that, through the previous calibration of the accessory, are transformed into normalized values (from 0 to 1). Results are obviously referred to the 100% corresponding to pure and fresh MgO.

Total transmittance measurements

As shown in Figure C1d, the mesh is placed to intercept the trajectory of the sample beam while keeping the MgO in the sample and the reference ports. Results provide the values of transmittance that through calibrations are transformed into normalized transmissions (from 0 to 1).

Calibrations and measurements are repeated for each wavelength of interest (in this case, every 10 nm from 290 nm to 390 nm).

Appendix D

To calculate "predicted" current intensities corresponding to outgoing fluxes, we must know, from the model, theoretical values of the outgoing spectral radiation fluxes ($q^{+}_{\lambda,\mathrm{mod}}$). To do it we must have the value of the incoming spectral radiation fluxes at the opposite window (q_{λ}^{0+}). This value can be obtained from type "a" measurements and the known spectral distribution of the lamp output power.

The space between the lamps and the window for radiation entry is transparent (no absorption or scattering). Then, the spectral radiation intensity in the forward direction on the reactor window (I_{λ}^{0+}) is proportional to the spectral distribution of the lamp output power (P_{λ})

$$\frac{I_{\lambda}^{0+}}{I^{0+}} = \frac{P_{\lambda}}{\int_{\lambda} P_{\lambda}\, d\lambda} = \frac{P_{\lambda}}{P} \tag{D1}$$

with

$$I^{0+} = \int_{\lambda} I_{\lambda}^{0+}\, d\lambda \tag{D2}$$

The output power distribution of the lamp resembles a normal curve with a maximum peak at 350 nm. Let us call this maximum value P_p and ϵ_{λ} the normalized spectral distribution of the lamp output power with respect to P_p. ϵ_{λ} can be obtained from the lamp manufacturer specifications or from special radiometric measurements. Then

$$\frac{P_{\lambda}}{P_p} = \epsilon_{\lambda} \tag{D3}$$

It follows that

$$\frac{I_{\lambda}^{0+}}{I^{0+}} = \frac{\epsilon_{\lambda}}{\int_{\lambda} \epsilon_{\lambda} d\lambda} \tag{D4}$$

From the definition of the radiation flux vector, the spectral (monochromatic) incoming radiation flux vector for the forward component corresponding to the k lamp is

$$\boldsymbol{q}_{k\lambda}^{0+} = \int_{\Omega} I_{k\lambda}^{0+}\, \hat{\boldsymbol{\Omega}}\, d\Omega \tag{D5}$$

Now consider M lamps ($k = 1, 2, 3, \ldots, M$) and a detector with a surface characterized by a unit normal vector entering the sensor equal to $\hat{\boldsymbol{n}}$ (Figure D1). The detector receives

$$q_{k\lambda}^{0+} = \boldsymbol{q}_{k\lambda}^{0+} \cdot \hat{\boldsymbol{n}} = I_{k\lambda}^{0+} \left[\int_{\Omega} \hat{\boldsymbol{\Omega}} \cdot \hat{\boldsymbol{n}}\, d\Omega \right]_k \tag{D6}$$

from this lamp.

The integral is extended over the solid angle of vision corresponding to the k-lamp–detector relative spatial distribution (defined by the detector position, the lamp position, and both the lamp and detector dimensions). For M lamps, the entering radiation flux to the detector is

$$q_{\lambda}^{0+} = I_{\lambda}^{0+} \sum_{k=1}^{M} \left[\int_{\Omega} \hat{\boldsymbol{\Omega}} \cdot \hat{\boldsymbol{n}}\, d\Omega \right]_k \tag{D7}$$

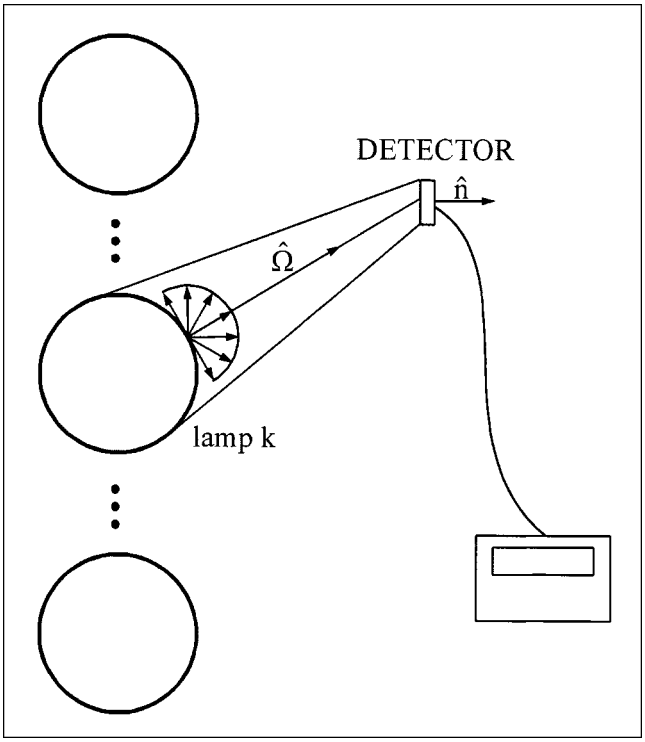

Figure D1. Detector vision solid angle, lateral view.

It is assumed that the M lamps are equal. Equation D7 can be integrated for all wavelengths

$$q^{0+} = \int_\lambda q_\lambda^{0+} d\lambda = \int_\lambda I_\lambda^{0+} \sum_{k=1}^{M} \left[\int_\Omega \hat{\boldsymbol{\Omega}} \cdot \hat{\boldsymbol{n}} \, d\Omega \right]_k d\lambda$$

$$= I^{0+} \sum_{k=1}^{M} \left[\int_\Omega \hat{\boldsymbol{\Omega}} \cdot \hat{\boldsymbol{n}} \, d\Omega \right]_k \quad \text{(D8)}$$

From Eqs. D4, D7, and D8

$$\frac{q_\lambda^{0+}}{q^{0+}} = \frac{\epsilon_\lambda}{\int_\lambda \epsilon_\lambda d\lambda} \quad \text{(D9)}$$

In Eq. D9, q_λ^{0+} is given in $\mathrm{W \cdot cm^{-2} \cdot nm^{-1}}$, because ϵ_λ is obtained from the manufacturing information obtained from radiometer measurements.

The current intensity detected by the radiation sensor is an integrated value for all wavelengths. Then, for the radiation field without windows and without catalytic meshes

$$i_{0,\mathrm{exp}} = \int_\lambda i_{0\lambda} d\lambda \quad \text{(D10)}$$

In Eq. D10, $i_{0\lambda}$ represents the current intensity per unit wavelength interval, associated with the spectral radiation flux q_λ^{0+}. Considering that the sensitivity of the radiation sensor is known

$$i_{0\lambda} = S(\lambda) q_\lambda^{0+} \quad \text{(D11)}$$

where $S(\lambda)$ represents the detector sensitivity in $\mathrm{A \cdot W^{-1} \cdot cm^2}$, which corresponds to wavelength λ. Then

$$i_{0,\mathrm{exp}} = \int_\lambda S(\lambda) q_\lambda^{0+} d\lambda \quad \text{(D12)}$$

Replacing q_λ^{0+} in Eq. D12 by its expression from Eq. D9, since $\int_\lambda \epsilon_\lambda d\lambda$ is independent of λ, we get

$$i_{0,\mathrm{exp}} = \frac{q^{0+} \int_\lambda S(\lambda) \epsilon_\lambda d\lambda}{\int_\lambda \epsilon_\lambda d\lambda} \quad \text{(D13)}$$

From Eqs. D9 and D13

$$q_\lambda^{0+} = i_{0,\mathrm{exp}} \frac{\epsilon_\lambda}{\int_\lambda S(\lambda) \epsilon_\lambda d\lambda} \quad \text{(D14)}$$

Transforming Eq. D14 into photochemical units with the $k \times \lambda$ factor (Brandi et al., 2000), we get

$$q_\lambda^{0+} = i_{0,\mathrm{exp}} \frac{\lambda \epsilon_\lambda k}{\int_\lambda S(\lambda) \epsilon_\lambda d\lambda} \quad \text{(D15)}$$

Now, in Eq. D15, q_λ^{0+} is expressed in $\mathrm{einstein \cdot s^{-1} \cdot cm^{-2} \cdot nm^{-1}}$.

Incorporating the peak sensitivity of the radiometer at 350 nm (S_p) into Eq. D14, we get

$$q_\lambda^{0+} = i_{0,\mathrm{exp}} \frac{\lambda \epsilon_\lambda k}{S_p \int_\lambda S_n(\lambda) \epsilon_\lambda d\lambda} \quad \text{(D16)}$$

where $S_n(\lambda)$ represent the normalized sensitivity of the radiometer provided by the manufacturer.

Appendix E

With the value of q_λ^{0+} (provided by Eq. D16) the model can calculate the spectral radiation fluxes $q_{\lambda,\mathrm{mod}}^{+}$ at any point inside the reactor, and consequently, also at the opposite window (with 0, 1, 2, …, N meshes inside the reaction space). To make a direct comparison, we would like to transform the predicted outgoing radiation fluxes into current intensities.

An equation identical to Eq. D12 can be applied to the model predictions

$$i_{\mathrm{mod}} = \int_\lambda S(\lambda) q_{\lambda,\mathrm{mod}}^{+} \, d\lambda \quad \text{(E1)}$$

Thus, Eq. E1 gives the current intensity that would be produced by the radiometer if the spectral radiation flux leaving the reactor (at the opposite window to that where the radiation enters) is $q^{+}_{\lambda,\mathrm{mod}}$. Units for $q^{+}_{\lambda,\mathrm{mod}}$ and S(λ) are in einstein $\cdot s^{-1} \cdot cm^{-2} \cdot nm^{-1}$ and $A \cdot \mathrm{einstein}^{-1} \cdot s \cdot cm^{2}$, respectively.

Transforming the values of $S(\lambda)$ into radiometric units ($A \cdot W^{-1} \cdot cm^{2}$) (Brandi et al., 2000)

$$i_{\mathrm{mod}} = \int_{\lambda} \frac{S(\lambda) q^{+}_{\lambda,\mathrm{mod}}}{k \times \lambda} d\lambda \qquad \text{(E2)}$$

This transformation is needed, because the spectral sensitivity of the radiometer provided by the manufacturer is expressed in radiometric units.

Finally, incorporating S_p into Eq. E2 one gets

$$i_{\mathrm{mod}} = \frac{S_p}{k} \int_{\lambda} S_n(\lambda) \frac{q^{+}_{\lambda,\mathrm{mod}}}{\lambda} d\lambda \qquad \text{(E3)}$$

Using Eq. E3, there is no need for making additional assumptions to compare predictions with experiments. This is not the case if we would like to compare outgoing fluxes with transformed experimental current intensities. To make this transformation, we must make assumptions concerning the spectral distribution of the experimental outgoing fluxes, because measured current intensities correspond to an integrated value over all wavelengths.

Manuscript received Mar. 6, 2001, and revision received Sept. 20, 2001.